Material and strain sensing uncertainties quantification for the shape sensing of a composite wing box

Material and strain sensing uncertainties quantification for the shape sensing of a composite wing box

Marco Esposito*[1,2] and Marco Gherlone[1]

[1] Department of Mechanical and Aerospace Engineering, Politecnico di Torino, Torino, Italy
[2] Aerospace Engineering and Aviation, RMIT University, Melbourne, Australia
* Correspondence: marco.esposito@polito.it

Abstract

The shape sensing, i.e. the reconstruction of the displacement field of a structure from discrete strain measures, is a key tool for the support and development of the modern Structural Health Monitoring frameworks and has received a huge attention in the last few decades. The parallel increase in the use of composite materials in the aerospace industry has consequently generated the need to investigate the applicability of the shape sensing methods to this peculiar kind of materials. In fact, the manufacturing complexity of the composite materials can result in a significant variability in the characteristics of the material. Therefore, a study on the propagation of this kind of uncertainty on the performance of the shape sensing methods is paramount. The uncertainties in the strain measurements can influence the shape sensing results and must be also considered. This paper, for the first time, investigates the propagation of these two sources of inputs' uncertainty on the performance of three shape sensing methods, the inverse Finite Element Method (iFEM), the Modal Method (MM) and the Ko's Displacement theory. Using the Monte Carlo Simulation (MCS) with Latin Hypercube Sampling (LHS), the robustness of the three methods with respect to the inputs' variability is evaluated on the reconstruction of the displacement field of a composite wing box. The MM shows a significant robustness and the iFEM, although more affected by the uncertainties, is the method that achieves the best accuracy. The Ko's displacement theory, on the other hand, is the less accurate and the less robust.

Keywords: Structural Health Monitoring; Shape sensing; Material characteristics uncertainty; Strain measurements uncertainty; Displacement field reconstruction.

Abbreviations:
The following abbreviations are used in this manuscript:

CoV	Coefficient of Variation
FEM	Finite Element Method
iFEM	inverse Finite Element Method
LHS	Latin Hypercube Sampling
MCS	Monte Carlo Simulation
MM	Modal Method
PDF	probability density function
SHM	Structural Health Monitoring

1 Introduction

Shape sensing techniques have witnessed a rapid development during the last few decades. These techniques allow the reconstruction of the full displacement field of a structure from discrete strain measurements. On a structure, strain measures are usually easily obtained through strain gauges and, more recently, by means of

fibre optics distributed strain sensing systems [1, 2]. The knowledge of the displacement field can provide key information for the application of the modern Structural Health Monitoring (SHM) frameworks. In fact, as recently proved in [3–6], the reconstruction of the displacement field can lead to the detection of damages in thin plates, stiffened plates and thin-walled cylindrical structures, using only few strain measures. Moreover, the reconstruction of the displacement field is fundamental for the monitoring of the morphing structures [7–9]. In particular, the knowledge of the actual structural shape can be used as a feedback control for the morphing mechanisms [10].

As already mentioned, a lot of interest and research effort has surrounded the development of the shape sensing technology. Different techniques, all having in common the use of discrete strains as an input, have been designed and tested on various problems. Three of them, based on different principles, have emerged so far as the most reliable and successful in the open literature: the Ko's Displacement theory [11], the Modal Method (MM) [12–14] and the inverse Finite Element Method (iFEM) [15].

The Ko's Displacement theory is based on the double integration of the curvature equation of the Bernoulli-Euler beam. Through this model, for beam-like structures, the curvature can be expressed as a function of the axial strains and of the distance of the measure from the neutral axis of the local section. Deriving the deflection from the curvature, it is possible to reconstruct the vertical displacement along a sensing line at the same locations where the strains are measured. The method was originally proposed in [11], numerically validated on the wing of the Ikhana Unmanned vehicle [16] and then experimentally applied on the Global Observer UAV [17] and, recently, on a cantilevered composite beam [18]. In [19], the method was specifically formulated for the use of strain measurements coming from distributed fibre optic sensors (FOS) and also tested on a cantilevered composite beam. In [20], the method was expanded in order to reconstruct the full displacement field of a beam-like structure. By means of a modal transformation [21, 22], the new formulation is able to expand the displacements reconstructed along the sensing lines to the displacements in locations outside of the sensing locations, allowing the reconstruction of the full displacement field. Using this novel formulation, the method requires the computation of the modal characteristics of the structure.

The Modal Method, firstly developed in [12, 13], is able to reconstruct the displacement field of any structure using its modal shapes and some discrete strain measures. The strain field is expressed in terms of known spatial functions, the modal strain shapes, and unknown weights, the modal coordinates. The modal coordinates are computed by fitting the reconstructed strain field to the discrete measured strains. Once the whole strain field is approximated, the displacement field is easily computed through the strain-displacements relations. In [12], the modal strain shapes were experimentally computed to reconstruct the displacement field of a cantilevered aluminum plate. Since the experimental evaluation of the modal strain properties can be really difficult, in [23] they were numerically computed and then adopted to reconstruct the deformation of a real plate. The study didn't include an evaluation of the error introduced by using the numerically computed modal shapes. Recently, in [24], the MM was experimentally validated on the reconstruction of the static and dynamic displacements of a wing.

The iFEM was introduced in [15]. Following the same approach of the direct FEM, the method uses a discretization of the structural domain with finite elements. Within each element the displacement field is expressed by the interpolation of the nodal values trough shape functions. The strain-displacement relationship is invoked to express the strain field in terms of the nodal displacements and of the spatial derivatives of the shape functions. By minimizing the error between the interpolated strain field and the discrete strains information coming from the strain sensors, the method is able to find the nodal displacements that best fit the measured strains. The IFEM has been successfully applied to a vast amount of applications. Truss and beam structures has been studied in [25, 26]. Three nodes inverse shell elements have been widely used for the analysis of thin plates [27–29] and thin walled structures [30, 31]. Recently, a quadrilateral inverse shell element, the IQS4, has been developed and broadly applied to marine structures [32–34]. The IQS4 elements have also been adopted in [35]. This study compared the three aforementioned shape sensing methods, the MM, the Ko's Displacement theory and the iFEM, on the numerical reconstruction of the full displacement field of a composite wing box. The most recent development in the field of iFEM is represented by the introduction

of an isogeometric formulation for variable cross-section beams [36] and curved shell structures [37]. In [38], a smoothing technique for the computation of the full strain field from discrete strain measures has further enriched the capabilities of the iFEM. The a priori expansion of few strain measures, inputs of the method, allows an accurate shape sensing with fewer strain measurements.

The use of composite materials is rapidly increasing in the aerospace industry due to their impressive specific mechanical properties and to the possibility to design tailored characteristics for a specific application. Nevertheless, they are also affected by uncertainties in their characteristics that can influence their behavior. The manufacturing of composites is complex and difficult to control. Therefore, the actual laminates characteristics can differ from the nominal ones. Fibre-to-matrix volume ratio, alignment of the fibres, temperature effects during the curing process, porosity in the matrix, bonding between fibres and matrix are factors that depend on the manufacturing process and that can introduce variability in the material properties [39]. The quantification of the effect of these uncertainties on the direct structural problem, i.e. strength, failure, buckling and stiffness analysis, is frequently performed by means of Monte Carlo Simulation (MCS) [40–42]. The MCS, when using simple sampling, requires a considerable amount of samples so that the outputs analysis can be considered representative of the variability of the inputs. The introduction of Latin Hypercube Sampling (LHS), firstly described in [43], allowed the reduction of the number of samples and has been recently adopted in the material uncertainty quantification study of laminated composites. In [44], the influence of the thickness, the ply orientation and the lamina characteristics on the linear static and vibration analysis of composite plates has been investigated using LHS. Lately, in [45], LHS has been used as the reference method to prove the accuracy of two other stochastic analysis methods (PCDD and COLL) for the uncertainty quantification of composite laminates.

As for the direct structural problem, the shape sensing methods are also influenced by the input uncertainties. Although experimental validation and comparison of the three methods is present in the open literature [46], a deep analysis of the effect of composite material characteristics uncertainties on the performance of the shape sensing methods is missing. Another uncertainty that can influence the performance of the shape sensing methods is due to the inaccuracy of the strain measurements. Several works have been dedicated to investigate the sources of biases (systematic errors) and uncertainties (random errors) affecting strain sensors (especially strain gauges) [47, 48]: temperature, transverse sensitivity of the sensor, misalignment, Wheatstone bridge's non-linearity. These effects are not taken into account systematically in this paper. Only the effect of noise on the ideal measured strains is analyzed. In [32, 49] a study of the influence of white noise in the strain inputs on the IFEM is present. Nevertheless, the study doesn't include the MM and The Ko's Displacements theory.

The scope of this paper is to continue the study on the composite wing box started in [35] and, for the first time, to evaluate and compare the effect of material and measurements uncertainties on the performance of the three shape sensing methods. The same combination of MCS and LHS, usually adopted for the direct structural problem, is used for the stochastic analysis of the three methods. The two kinds of uncertainties are treated separately. This analysis proves that, although the MM is more robust and less influenced by the inputs' uncertainties, it is not capable of a better accuracy than the iFEM, also when the uncertainties have the most negative effect on its performances. Moreover, the Ko's Displacement theory results to be the less robust method with respect to the inputs' uncertainties. The paper is structured as follows. In section 2, the shape sensing methods are briefly described. In section 3, the deterministic shape sensing of the wing box, not affected by any uncertainty, is presented. Section 4 defines the methodology adopted for the uncertainty analysis and the results of this analysis are reported in section 5. Finally, the concluding remarks are discussed in section 6.

2 Shape sensing methods

In this section, the three shape sensing methods, as they have been adopted in this work, are briefly described. A more detailed description of the methods can be found in [35, 46].

2.1 Modal Method

When discretizing a structural domain using a FE model, both the displacements and the strains of the structure can be expressed in terms of a modal matrix and the vector of the modal coordinates

$$\boldsymbol{w} = \boldsymbol{\Phi}_d \, \boldsymbol{q} \tag{1}$$

$$\boldsymbol{\varepsilon} = \boldsymbol{\Phi}_s \, \boldsymbol{q} \tag{2}$$

where $\boldsymbol{w}_{Dx1}$ is the nodal degrees-of-freedom (DOFs) vector and $\boldsymbol{\varepsilon}_{Sx1}$ is the strains vector. The modal matrix $[\boldsymbol{\Phi}_d]_{DxM}$ is constituted by M columns (the i-th column being the i-th modal eigenvector of the displacement degrees-of-freedom). The modal matrix $[\boldsymbol{\Phi}_s]_{SxM}$ is also constituted by M columns (the i-th column being the i-th set of strains corresponding to the i-th mode shape of the FE model of the structure). The modal coordinates that best fit, in a least square sense, the strain field to the discrete strains vector can be computed by pseudo-inverting Equation 2

$$\boldsymbol{q} = (\boldsymbol{\Phi}_s^T \boldsymbol{\Phi}_s)^{-1} \boldsymbol{\Phi}_s^T \, \boldsymbol{\varepsilon} \tag{3}$$

Substituting (3) into (1) leads to the expression of the nodal DOFs in terms of the modal matrices and the discrete strains [12, 13]

$$\boldsymbol{w} = \boldsymbol{\Phi}_d (\boldsymbol{\Phi}_s^T \boldsymbol{\Phi}_s)^{-1} \boldsymbol{\Phi}_s^T \, \boldsymbol{\varepsilon} \tag{4}$$

The nodal DOFs can then be computed by substituting ε with discrete strain measurements. This procedure is possible only if the number of available strains (S) is greater or equal to the number of considered modes (M). No mathematical restriction is imposed on the number of the desired DOFs (D).

2.2 Ko's Displacement theory

The Ko's Displacement theory [11] is based on the Bernoulli-Euler beam theory. According to this model, the curvature along the beam axial coordinate p can be expressed as follows:

$$w_{,pp}(p) = -\varepsilon(p)/z \tag{5}$$

where z is the distance between the neutral axis and the strain sensor and ε is the strain measured along the p direction.

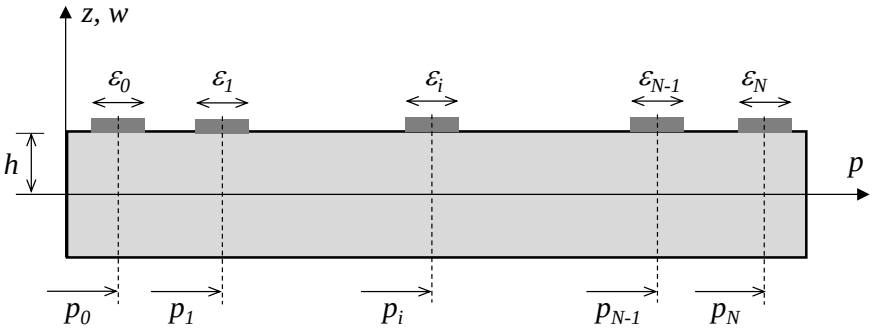

Figure 1: Ko's Displacement theory - Geometry and sensors' location.

Double integration of the curvature, assuming that N+1 strain measurements (ε_0, ε_1, ... ε_N) are available along p at $p = p_0, p_1, ..., p_N$, respectively (Figure 1), that strain is linear between any two consecutive locations and that strains sensors are located at a constant distance from the neutral axis ($z = h$), leads to the expression of the deflection of the beam at the i-th station where the strain is measured [46]:

$$w_i = -\frac{1}{6h}\left[\sum_{j=1}^{i}(2\varepsilon_{j-1}+\varepsilon_j)(p_j-p_{j-1})^2 + 3\sum_{k=1}^{i-1}(\varepsilon_{k-1}+\varepsilon_k)(p_k-p_{k-1})(p_i-p_k)\right] \quad (i=1,2,...,N) \tag{6}$$

This formulation is valid for clamped end boundary conditions at $p = p_0$. More general formulations, that can face different conditions, have been also derived [11].

Using a two step procedure, where the first step is represented by the computation of the deflections along the strain sensing lines, as described by Equation (6), it is possible to extend the displacement reconstruction to all the DOFs of a beam-like structure [20]. During the second step, the deflections computed in the previous one are used as *master* DOFs ($\boldsymbol{w}_m$) to expand the shape sensing to the desired, or *slave*, DOFs ($\boldsymbol{w}_s$). The expansion is obtained by means of the System Equivalent Reduction and Expansion Process (SEREP) [21]:

$$\boldsymbol{w} = \begin{Bmatrix}\boldsymbol{w}_m \\ \boldsymbol{w}_s\end{Bmatrix} = \begin{bmatrix}\boldsymbol{\Phi}_{dm}(\boldsymbol{\Phi}_{dm}^T\boldsymbol{\Phi}_{dm})^{-1}\boldsymbol{\Phi}_{dm}^T \\ \boldsymbol{\Phi}_{ds}(\boldsymbol{\Phi}_{dm}^T\boldsymbol{\Phi}_{dm})^{-1}\boldsymbol{\Phi}_{dm}^T\end{bmatrix}\ \boldsymbol{w}_m \tag{7}$$

where $[\boldsymbol{\Phi}_{dm}]_{D_m x M}$ is the master DOFs modal shapes matrix, $[\boldsymbol{\Phi}_{ds}]_{D_s x M}$ is the slave DOFs modal shapes matrix, D_m is the number of master DOFs, D_s is the number of slave DOFs and M is the number of the retained modes. The expansion obtained through SEREP allows the reconstruction of the full displacement field, but it involves the use, and consequently the computation, of the modal shapes of the structure.

2.3 iFEM

The inverse Finite Element Method has been inspired by the direct FEM [15]. The displacement field is expressed in terms of the kinematic variables according to a specific structural model. In this application, since the objective of the analysis is a thin-walled structure, the First Order Shear Deformation Theory has been adopted [50]. Therefore, the displacement field can be expressed in terms of the plate's reference surface in-plane displacements, u and v, the transverse displacement w and the rotations around the mid-plane axis x and y, expressed by θ_x and θ_y, respectively. Accordingly, the strain field can also be expressed in terms of the

derivatives of the kinematic variables [15, 50]:

$$\begin{Bmatrix} \varepsilon_{xx} \\ \varepsilon_{yy} \\ \gamma_{xy} \end{Bmatrix} = \begin{Bmatrix} u_{,x} \\ v_{,x} \\ v_{,x} + u_{,y} \end{Bmatrix} + z \begin{Bmatrix} \theta_{y,x} \\ -\theta_{x,y} \\ (\theta_{y,y} - \theta_{x,x}) \end{Bmatrix} = \mathbf{e} + z\mathbf{k} \tag{8a}$$

$$\begin{Bmatrix} \gamma_{xz} \\ \gamma_{yz} \end{Bmatrix} = \begin{Bmatrix} w_{,x} + \theta_y \\ w_{,y} - \theta_x \end{Bmatrix} = \mathbf{g} \tag{8b}$$

Therefore, the strain field of FSDT can be fully described by the eight strain measures ε_k $(k = 1, 2, ..., 8)$:

$$\mathbf{e} = [u_{,x},\ v_{,x},\ v_{,x} + u_{,y}]^T = [\varepsilon_1,\ \varepsilon_2,\ \varepsilon_3]^T \tag{9a}$$

$$\mathbf{k} = k = [\theta_{y,x},\ -\theta_{x,y},\ \theta_{y,y} - \theta_{x,x}]^T = [\varepsilon_4,\ \varepsilon_5,\ \varepsilon_6]^T \tag{9b}$$

$$\mathbf{g} = [w_{,x} + \theta_y,\ w_{,y} - \theta_x]^T = [\varepsilon_7,\ \varepsilon_8]^T \tag{9c}$$

Once the kinematic model is established, the domain is discretized using FE and the kinematic variables inside each element are interpolated using shape functions:

$$[u,\ v,\ w,\ \theta_x,\ \theta_y]^T = \mathbf{N}\mathbf{u}^e \qquad (\mathbf{u}^{eT} = \{u_i,\ v_i,\ w_i,\ \theta_{xi},\ \theta_{yi}\},\ i = 1, 2, ..., S) \tag{10}$$

where $\mathbf{N}$ is the shape functions matrix, $\mathbf{u^e}$ is the vector of the element's nodal DOFs and S is the number of the element's nodes. $\mathbf{N}$ and S depend on the chosen element formulation. Throughout this paper, iQS4 four-nodes elements are used, therefore, $S = 4$. The detailed formulation of the shape functions can be found in [32].

Substituting Eq. (10)into definitions (9), the k-th strain measure can be expressed in terms of the spatial derivatives of the shape functions and the nodal DOFs:

$$\varepsilon_k(\mathbf{u}^e) = \mathbf{B}_k\mathbf{u}^e \quad (k = 1,\ 2,\ ..., 8) \tag{11}$$

where $\mathbf{B}_k$ is the matrix containing the derivatives of the shape functions related to the k-th strain measure. The detailed formulation of $\mathbf{B}_k$ for can also be found in [32].

The objective of inverse Finite Element Method is to find the nodal DOFs values that minimize the error between the strain field, as expressed in (11), and the one measured in a finite number of discrete locations. The error within each element is expressed through a least-square functional defined as follows [51]:

$$\Psi^e(\mathbf{u}^e) = \sum_{k=1}^{8} \lambda_k^e w_k^e \iint_{A^e} (\varepsilon_k(\mathbf{u}^e) - \varepsilon_k^\varepsilon)^2 dxdy \tag{12}$$

The superscript ε denotes an experimentally measured value. The argument of the integral over the element's area, A_e, is the squared difference between the experimentally evaluated strain measure, $\varepsilon_k^\varepsilon$, and its analytical counterpart, $\varepsilon_k(\mathbf{u}^e)$, depending on the element nodal DOFs. In the case of sparse strain sensors, the absence of the k-th strain measure within an element is taken into account by setting the experimental strain measure to zero and by setting the penalization factor λ_k^e to a small value (10^{-4}). Otherwise, if the k-th strain measure has been experimentally evaluated in the element, the related λ_k^e is set to be equal to 1. Since the transverse shear strains are not measurable, the $\lambda_{7,8}^e$ are always equal to 10^{-4} and the $\varepsilon_{7,8}^\varepsilon$ are equal to 0. The w_k^e are dimensional coefficients required to guarantee the physical units consistency of Eq. (12). They are set as follows: $w_k^e = 1$ for $k = 1, 2, 3, 7, 8$ and $w_k^e = (2h)^2$ for $k = 4, 5, 6$, where h is the half-thickness of the element.

The integrals in (12) are numerically computed using the Gaussian quadrature, therefore they are trans-

formed into summations over the nxn Gauss points [35]:

$$\iint_{A^e} (\varepsilon_k(\mathbf{u}^e) - \varepsilon_k^{\varepsilon})^2 dxdy = \sum_{i=1}^{nxn} \chi_i \omega_i (\varepsilon_{k(i)}(\mathbf{u}^e) - \varepsilon^{\varepsilon}_{k(centroid)})^2 \qquad \begin{pmatrix} \chi_{i=centroid} = 1 \\ \chi_{i \neq centroid} = 10^{-4} \end{pmatrix} \tag{13}$$

where ω_i are the quadrature weights, the subscript i denotes the computation of the quantity in the i-th quadrature point and the subscript *centroid* refers to the quantity computed in the centroid of the element. This formulation is designed to deal with the case where only one sensor is present in the element and it is located at its centroid, where a Gauss point is always present if nxn is even. Consequently, a second weight, χ_i, is introduced to penalize the contributes that come from quadrature points different from the centroid, where the strain is not actually measured [35]. Since the χ_i weights are introduced to take into account the exact location of the strain sensors, they are adopted only when a measure is present within the element. Therefore, for $k = 7, 8$ and for elements without sensors, only the penalization strategy introduced by λ_k^e is adopted.

The first six strain measures can be experimentally measured in the centroid of the element by strain sensors placed on the bottom $(-)$ and top $(+)$ surface of the plate:

$$\begin{Bmatrix} \varepsilon_1^e \\ \varepsilon_2^e \\ \varepsilon_3^e \end{Bmatrix}_{(centroid)} = \frac{1}{2} \begin{Bmatrix} \varepsilon_{xx}^+ + \varepsilon_{xx}^- \\ \varepsilon_{yy}^+ + \varepsilon_{yy}^- \\ \gamma_{xy}^+ + \gamma_{xy}^- \end{Bmatrix}_{(centroid)} \tag{14a}$$

$$\begin{Bmatrix} \varepsilon_4^e \\ \varepsilon_5^e \\ \varepsilon_6^e \end{Bmatrix}_{(centroid)} = \frac{1}{2h} \begin{Bmatrix} \varepsilon_{xx}^+ - \varepsilon_{xx}^- \\ \varepsilon_{yy}^+ - \varepsilon_{yy}^- \\ \gamma_{xy}^+ - \gamma_{xy}^- \end{Bmatrix}_{(centroid)} \tag{14b}$$

The procedure is completed with the minimization of the error functional in (12) with respect to the DOFs, thus leading to a system of linear equations that can be solved to find the nodal DOFs of the element:

$$\frac{\partial \Psi_e(\mathbf{u}^e)}{\partial \mathbf{u}^e} = \mathbf{k}^e \mathbf{u}^e - \mathbf{f}^e = 0 \tag{15a}$$

$$\mathbf{u}^e = \mathbf{k}^{e-1} \mathbf{f}^e \tag{15b}$$

where:

$$\mathbf{k}^e = \sum_{k=1}^{8} \sum_{i=1}^{nxn} [\lambda_k^e w_k^e \chi_i \omega_i \mathbf{B}_{k(i)}^T \mathbf{B}_{k(i)}] \tag{16a}$$

$$\mathbf{f}^e = \sum_{k=1}^{8} \sum_{i=1}^{nxn} [\lambda_k^e w_k^e \chi_i \omega_i \mathbf{B}_{k(i)}^T \varepsilon^{\varepsilon}_{k(centroid)}] \tag{16b}$$

The subscript i related to the $\mathbf{B}_k$ matrices denotes the computation of the matrix in the i-th Gauss point. It is important to notice once again that, if no measure is present within the element or $k = 7, 8$, the χ_i coefficient should be not considered in the previous formulas. On the other hand, if the measure is present, the value of χ_i is attributed following the rule expressed in (13).

The extension of the procedure to all the elements of the domain, trough the assembly process, leads to the system of linear equations for the global DOFs of the structure, $\mathbf{U}$:

$$\mathbf{U} = \mathbf{K}^{-1} \mathbf{F} \tag{17}$$

where $\mathbf{K}$ is a matrix depending on the shape functions and strain-sensor locations, whereas $\mathbf{F}$ is a vector incorporating the measured strains. The matrix $\mathbf{K}$ is a well-conditioned square matrix that, upon enforcement of the displacement boundary conditions, can be inverted. Assuming that the strain-sensor locations is not changed, the inversion of $\mathbf{K}$ is performed only once whereas the vector $\mathbf{F}$ needs to be updated at each strain-data acquisition increment. Since only strain-displacement relations are invoked in the formulation, the method does not require the knowledge of the material properties or the applied loads. Thus, it is applicable for both static and dynamic loading conditions, without requiring inertial or damping material properties.

3 Deterministic shape sensing

The structure, object of this shape sensing study is, the wing box model illustrated in Figure 2. The wing box is divided into two bays by two ribs. Four T-shaped stiffeners are present, two located on the top and two on the bottom panel. The upper and lower panel are connected to the spars by means of four L-shaped caps. The root section ($y = 0$) of the box is clamped and, at the tip section ($y = 1600$), a trapezoidal distributed load, with $q = 16\ N/mm$, is applied. This configuration guarantees a deformation with both bending and torsion, resulting in a challenging problem for the shape sensing techniques.

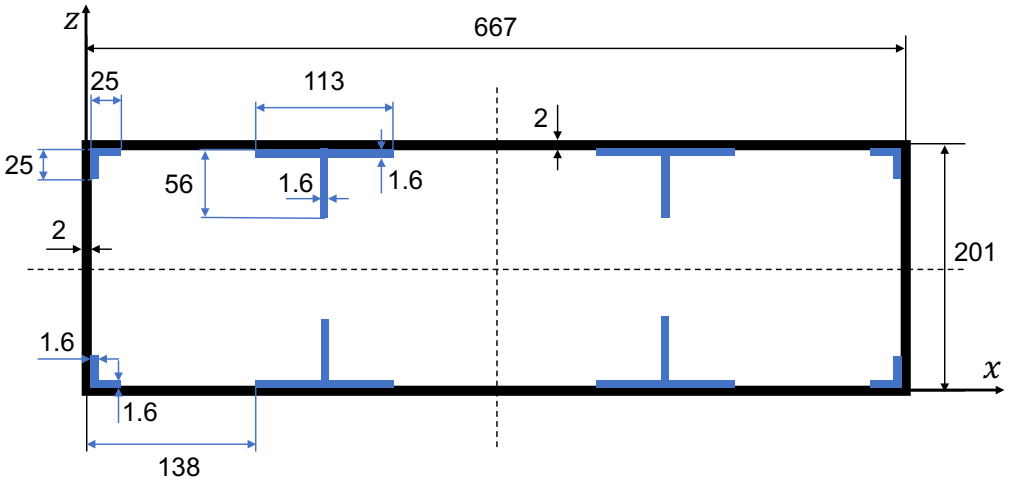

a) Cross section

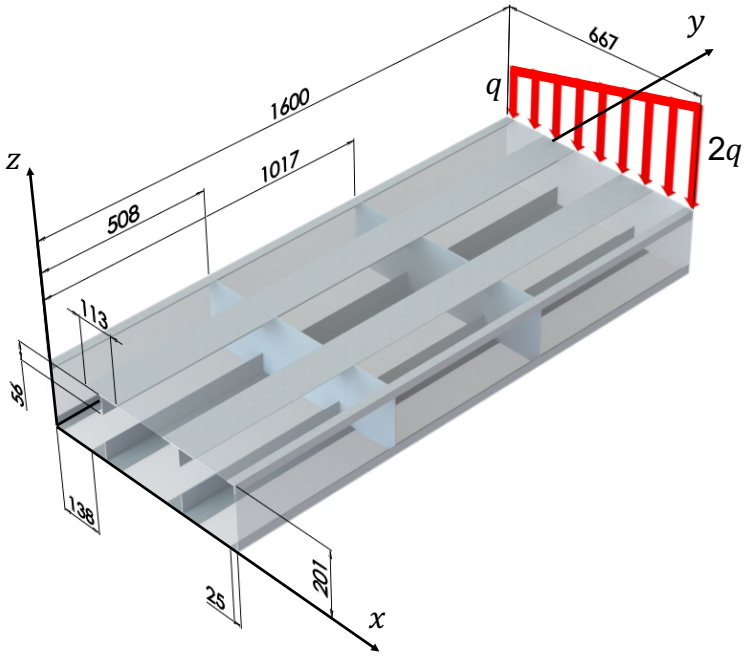

b) Isometric view

Figure 2: Geometry, boundary and loading conditions of the unswept wing box. - The wing box has a constant cross section (a), is divided into two bays by two ribs and a trapezoidal distributed load is applied at the tip section (b). The root section is clamped. All dimensions are expressed in mm.

A high-fidelity NASTRAN® FE model of the wing box was designed in order to generate the input strain values for the shape sensing methods and the reference displacements objective of the reconstructions. The same model was adopted for the computation of the modal properties of the structure (mode shapes and related strains), necessary for the application of the Ko's Displacements theory and of the Modal Method. The mesh of the model consisted of 21004 CQUAD4 elements. Figure 3 shows the wing box deformed shape (object of the displacement field reconstruction) as obtained with the high-fidelity FEM analysis. A coarser mesh was developed for the application of the iFEM, using iQS4 quad elements. The mesh was designed so that every centroid of the 1427 iQS4 elements was coincident with a node of the high-fidelity mesh.

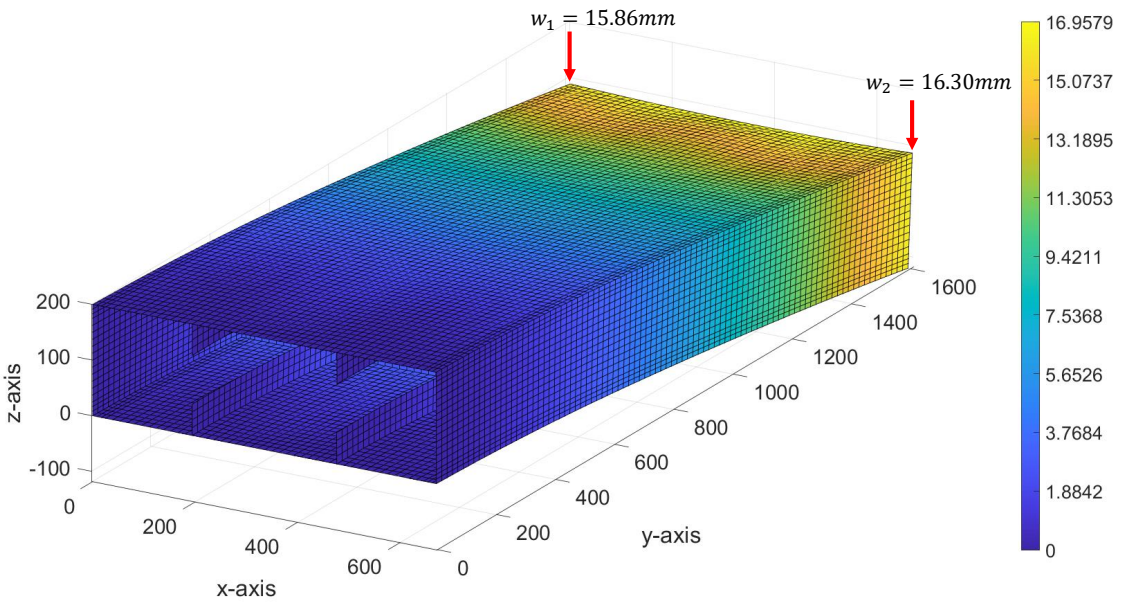

Figure 3: Wing box deformed shape as obtained with the FEM analysis - The color bar refers to the magnitude (in mm) of the resultant displacements, w_1 and w_2 represent, respectively, the vertical displacement of the top-left and top-right vertex of the tip cross section.

This phase of the study involved the use of composite materials with the properties of each ply (fibre orientation and thickness) supposed to be deterministic and equal to the nominal values reported in Table 1. The stacking sequence and the lamina properties are the same for each component of the box. The thickness of the plies for the skin and spars is set to 0.25 mm ($t_{(skin\ spars)}$), whereas the ply thickness of the remaining components is set to 0.20 mm (t).

Table 1: Deterministic material properties of a carbon-epoxy unidirectional ply [35].

Characteristic	**Nominal value**
$E_{11}[GPa]$	111
$E_{22}[GPa]$	7.857
ν_{12}	0.34
$G_{12}[GPa]$	3.292
$G_{13}[GPa]$	3.292
$G_{23}[GPa]$	3.292
$St.seq.$	$[45/-45/0/90]_s$
$t_{(skin\ spars)}[mm]$	$[0.25/0.25/0.25/0.25]_s$
$t[mm]$	$[0.20/0.20/0.20/0.20]_s$

The number of sensors and their location strongly influence the performances of the shape sensing techniques. The optimization of these two aspects has been the focus of a previous work [35]. A broad sensors configuration optimization campaign for iFEM, Ko's Displacement theory and Modal Method has been carried on using a Genetic Algorithm. All the three methods and the Genetic Algorithm have been implemented using in-house codes written in MATLAB®. The objective of the optimization has been the minimization of the RMS percent error between the reference vertical displacements and the reconstructed ones:

$$\%ERMS_w = 100 \times \sqrt{\frac{1}{n}\sum_{i=1}^{n}\left(\frac{w_i - w_i^{ref}}{w_{max}^{ref}}\right)^2} \tag{18}$$

where n is the number of nodes of the iFEM mesh, w_i^{ref} is the reference vertical displacement from the high-fidelity model in the i-th node's location, w_{max}^{ref} is the maximum reference vertical displacement and w_i is the reconstructed vertical displacement in the i-th node. The investigation has also covered the selection of the modes to be considered in the application of the MM and the Ko's Displacement theory. The 1st the 3rd and the 26th modes have been found to be the more significant for the modal representation of the investigated deformation. The final scope of the optimization was to compare the three methods, when applied to the same problem, each one at its best. Therefore, each optimized sensors configuration is different and it is the one that allows the corresponding method to reconstruct the wing box displacement field with the highest degree of accuracy.

The results of this investigation are summarized in Table 2. The results are reported in terms of the $ERMS_w$, the number of single strain gauges in the x_{str} direction (Sg_x) and the number of the three-components strain rosettes (R_{xy}) for the three methods.

Table 2: Deterministic shape sensing results.

	Ko	**MM**	**iFEM**
$ERMS_w$ [%]	6.9	4.8	**1.8**
Sg_x	28	33	
R_{xy}		40	108
S_{tot}	**28**	153	324

The detailed sensors configurations are represented in Figure 4, where also the measurement directions x_{str} and y_{str} are shown for the different wing box components. The configurations described here are the same ones reported in [35] with the exception of the one related to the Modal Method. For this method, a configuration with a slightly smaller amount of sensors, but with the same value of the $ERMS_w$, is adopted here.

Considering the practical difficulties connected with the application of sensors inside the wing box, only strains measured on the external surface were considered. Therefore, for the computation of the strain measures in Eqs. (14), constant values of the strains through the thickness of each plate were considered. This approximation is acceptable if the thickness of the skin panels is considerably smaller than the one of the entire wing box. For the Ko's Displacement theory, the optimizer was allowed to select only sensors aligned with the wing's longitudinal axis on the top and bottom skins of the box. In fact, the method's formulation requires the use of consecutive strain measurements aligned along the beam-like structure's longitudinal axis, at a given distance from its neutral axis. This constraint was not necessary for the iFEM and the MM, thus also sensors on the spars were allowed. Nevertheless, the optimizer exclusively selected sensors on the skin panels, not only for the Ko's Displacement theory, but also for the MM. On the other hand, only sensors on the spars were selected for the iFEM.

The different numbers of sensors for each method are a result of the optimization process. The genetic optimizer was set to select among a maximum of 324 sensor locations but it could also select the same location more than once, thus reducing the effective number of used strain information. Nevertheless, it is important to highlight that the previous study also proved that increasing the number of sensors to the amount used by the iFEM was ineffective for the MM and detrimental for the Ko's Displacement theory.

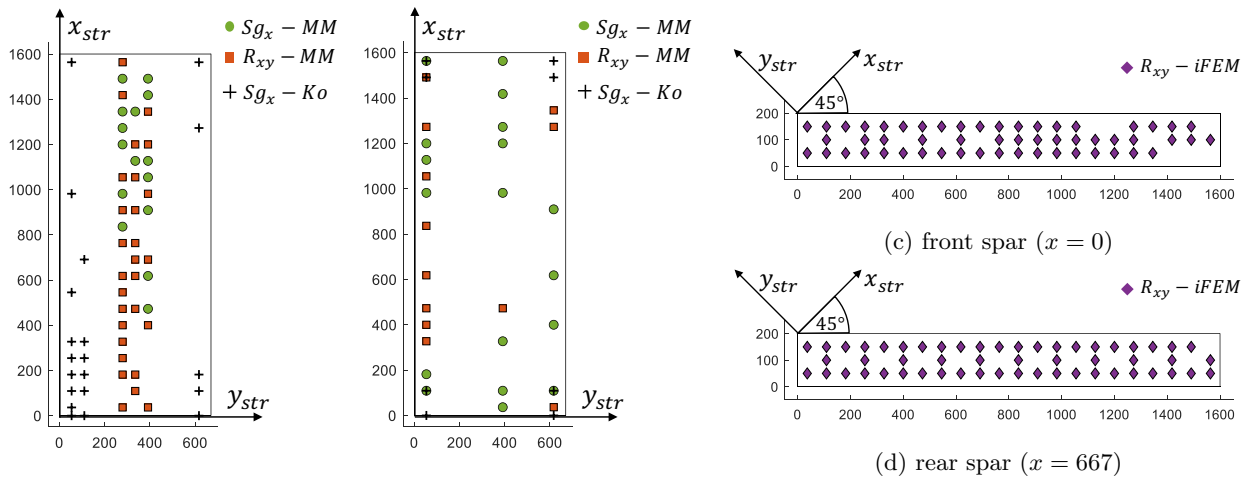

(a) upper skin ($z = 201$) (b) lower skin ($z = 0$)

(c) front spar ($x = 0$)

(d) rear spar ($x = 667$)

Figure 4: Sensors configurations - The optimization process for the three shape sensing methods selected sensors on the two skins for the MM and the Ko's Displacement theory (a)(b). For the iFEM, only sensor on the spars were selected (c)(d).

4 Uncertainty propagation analysis

The scope of this work is to study the propagation of uncertainties from the input data to the results of the shape sensing methods. This investigation aims at evaluating the reliability and robustness of the three methods when uncertainty affects the structural behavior, like in real case scenarios. The uncertainty quantification process consists in studying the output's probability density function (PDF) and its statistical moments when the inputs are subjected to variability. The more widely used method to perform this kind of analysis is the Monte Carlo Simulation (MCS). According to this method, a probability distribution is associated to each input variable. Several values of each variable are sampled from the assumed probability distribution in order to obtain several input vectors for the investigated model. The sampled input vector are then used to repetitively run the model, in this case the shape sensing methods, thus obtaining the PDF of the output. The number of input vectors influences the ability to obtain a PDF capable to fully describe the phenomenon. When simple random sampling is used, the required number of input vectors is large and, consequently, the computational time for the simulation is significant. The use of different sampling methods can increase the accuracy of the simulation with a smaller number of input vectors. Latin Hypercube Sampling (LHS) is a stratified sampling method that guarantees that all the portions of the distributions of each variable are represented in the sampling [52]. This guarantees a better accuracy with a small number of samples.

The input data for the shape sensing are the strain measurements. With respect to a deterministic simulation, these quantities can be affected by two kinds of uncertainties: uncertainties due to the material properties' variability and uncertainties affecting the experimental measurements. In this work, these two effects are treated separately.

4.1 Material uncertainty

The material uncertainties influence the strain field of the structure. In this paper, the material uncertainties are analyzed at the laminates' ply level, including the mechanical characteristics and the geometric ones. The ply mechanical properties' variability is modeled with normal distributions, having the mean values (μ) equal to the nominal ones and a Coefficient of Variation (CoV) of 7.5% [44]. The same distribution is used to represent the thickness of the plies. The fibre orientations are modeled with normal distributions with μ equal to the nominal ply angle and a standard deviations (σ) of 3° [53]. The variability represented by the distributions simulates the uncertainty that can originate from multiple sources. The deviation from the nominal values due

to the complexity of the manufacturing process, the variation of the material properties due to the fluctuation in the ambient conditions and other sources that can influence the composite behavior are all taken into account by the generous level of variability selected for the stochastic distributions of the variables.

Seven different stacking sequences are considered. The sequences share the same nominal values, but their characteristics are sampled separately so that a wider variability of the characteristics over the wing box's components can be obtained. The seven layups distribution on the wing box is illustrated in Figure 5.

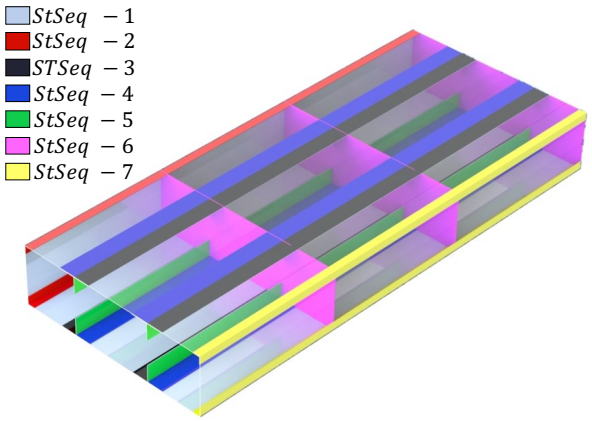

Figure 5: Stacking sequences - The box is divided into seven zones for the stochastic analysis. They have the same nominal stacking sequence but they are sampled separately in order to guarantee a higher degree of variability of the characteristics over the structure.

For every input vector of the MCS, the six mechanical properties are sampled once and associated to every ply in the structure. The symmetry of the layups, in terms of fibre orientation and thickness, is preserved also in the stochastic analysis. Therefore, four fibre orientations and four thicknesses are sampled for each of the seven layups. As a consequence, each input vector of the MCS is constituted by 62 input variables (4 fibre orientation x 7 stacking sequences, 4 ply thicknesses x 7 stacking sequences and 6 mechanical properties). The sampling of the variables is obtained using a LHS from the multivariate normal distributions previously illustrated and summarized in Table 3.

Table 3: Stochastic material characteristics.

Characteristic	**Distribution**	$\boldsymbol{\mu}$	$\boldsymbol{\sigma}$
$E_{11}[GPa]$	Normal	111	7.5% μ
$E_{22}[GPa]$	Normal	7.857	7.5% μ
ν_{12}	Normal	0.34	7.5% μ
$G_{12}[GPa]$	Normal	3.292	7.5% μ
$G_{13}[GPa]$	Normal	3.292	7.5% μ
$G_{23}[GPa]$	Normal	3.292	7.5% μ
$St.seq._{(StSeq\ 1-7)}$	Normal	$[45/-45/0/90]_s$	3°
$t_{(StSeq\ 1)}[mm]$	Normal	$[0.25/0.25/0.25/0.25]_s$	7.5% μ
$t_{(StSeq\ 2-7)}[mm]$	Normal	$[0.20/0.20/0.20/0.20]_s$	7.5% μ

Once a representative number of input vectors is extracted, the material characteristics of each vector are associated to the high-fidelity FE model and the stochastic strain measures are easily obtained, for each input vector, through direct FEM analysis. Each input vector's strain measures are subsequently used as inputs for the application of the iFEM, the Modal Method and the Ko's Displacement theory to obtain the PDF of the output, i.e., the $ERMS_w$. When computing the $ERMS_w$, the reference displacements are the one obtained from

the FEM analysis of the correspondent input vector. On the other hand, the Modal characteristics, necessary for the application of the MM and Ko's Displacement theory, are the ones obtained from the deterministic FE model (where all of the properties are set to the nominal values). This approach is based on the assumption that the modal properties, especially the one related to the strains, are really difficult to measure experimentally. Therefore, the idea is to simulate the most common case, i.e., the modal analysis is performed on the numeric model, whereas the strains and the displacements are measured experimentally and are affected by uncertainty. The entire process for n input vectors is schematized in Figure 6.

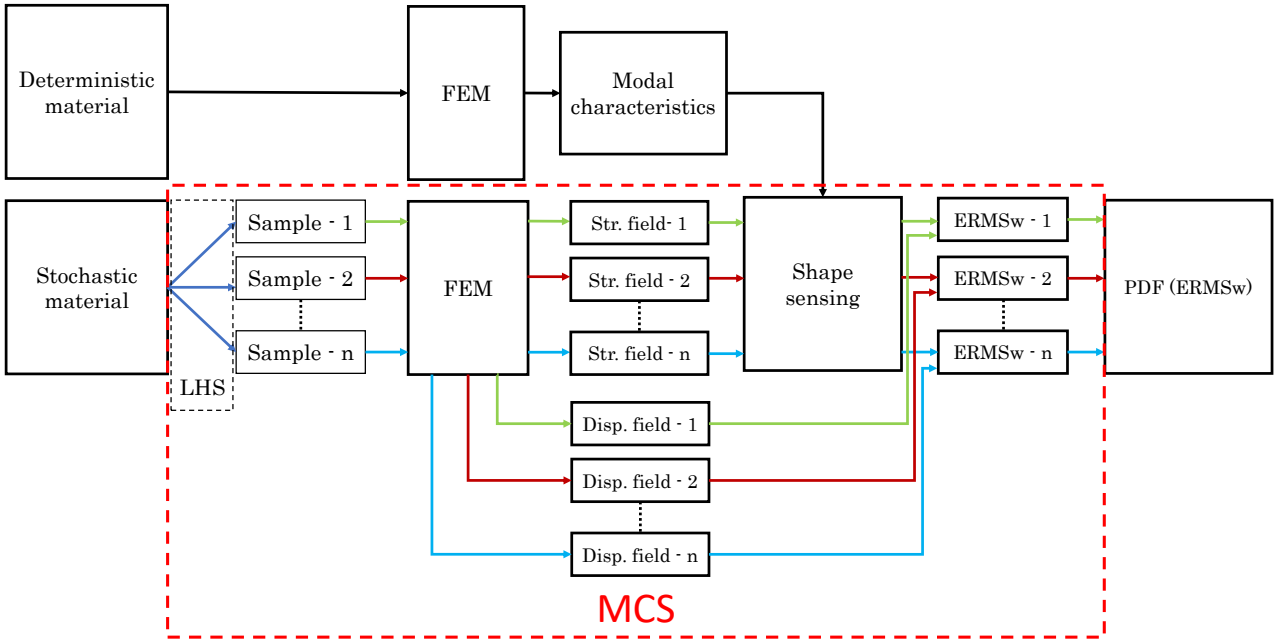

Figure 6: Material uncertainty simulation - The scheme illustrates the MCS with LHS procedure for the analysis of the material uncertainties.

4.2 Measurements uncertainty

The second scenario concerns the evaluation of the uncertainties that originate from the experimental measures of the strains. To take into account the deviation from the deterministic values caused by noisy strain measurements, two cases of normally distributed errors with zero mean and a standard deviation of 5% and 10% of the nominal value are added to the strain values obtained from the deterministic FEM analysis. All the input strain measurements used for the shape sensing techniques exhibit the distribution summarized in Table 4. In this case, the number of variables that constitute the input vectors depends on the number of strain sensors required by each shape sensing method.

Table 4: Stochastic strain measurements.

Characteristic	**Distribution**	$\boldsymbol{\mu}$	$\boldsymbol{\sigma}$
ε	Normal	Deterministic value	$5-10\%\ \mu$

The MCS procedure is similar to the one described in the previous section. The stochastic strains are sampled using the LHS and then the shape sensing techniques are applied to the obtained input vectors. Thus, the PDFs of the $ERMS_w$s are derived. The necessary modal properties are the ones evaluated from the deterministic FE model and, this time, the reference displacements also derive from this model. In fact, if the aim is to evaluate the uncertainty due to noisy strain measurements only, the hypothesis is that the real structure is supposed to behave like the deterministic one and the experimental strains are affected by measurement errors. The scheme

of the simulation is reported in Figure 7.

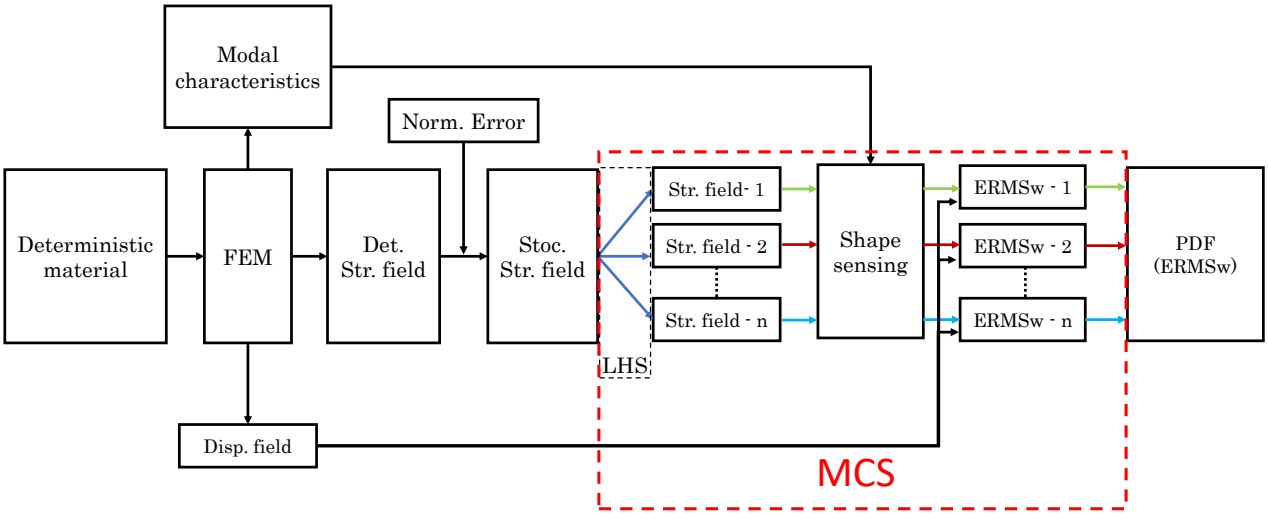

Figure 7: Measurements noise effect simulation - The scheme illustrates the MCS with LHS procedure for the analysis of the measurements uncertainties.

5 Results

The results from the material uncertainty analysis are presented in Figure 8. The results were extracted using 10000 input vectors. A convergence study to prove that this number of samples was able to characterize the output variability was performed. The result of the study showed that no variation for the value of the means and a maximum variation of 6% was observed for the CoV when increasing the number of samples to 20000 and 30000. These results are summarized in Table 5.

Table 5: Convergence study - The table shows the negligible variation of the CoV and of the μ of the $ERMSw$ distributions associated with the increase in the size of the input vectors.

	Material uncertainty			**Measurements uncertainty (5%)**			**Measurements uncertainty (10%)**		
	n=10000	**n=20000**	**n=30000**	**n=30000**	**n=50000**	**n=70000**	**n=30000**	**n=50000**	**n=70000**
Ko									
CoV	0.0873	0.0874	0.0878	0.0818	0.0817	0.0817	0.155	0.155	0.155
μ	7.208	7.208	7.208	6.971	6.971	6.971	7.199	7.199	7.199
MM									
CoV	0.0344	0.0365	0.0354	0.00422	0.00424	0.00416	0.0163	0.0164	0.0161
μ	4.937	4.937	4.937	4.839	4.839	4.839	4.883	4.883	4.883
iFEM									
CoV	0.117	0.118	0.117	0.156	0.156	0.156	0.291	0.290	0.289
μ	1.939	1.939	1.939	1.851	1.851	1.851	1.901	1.901	1.901

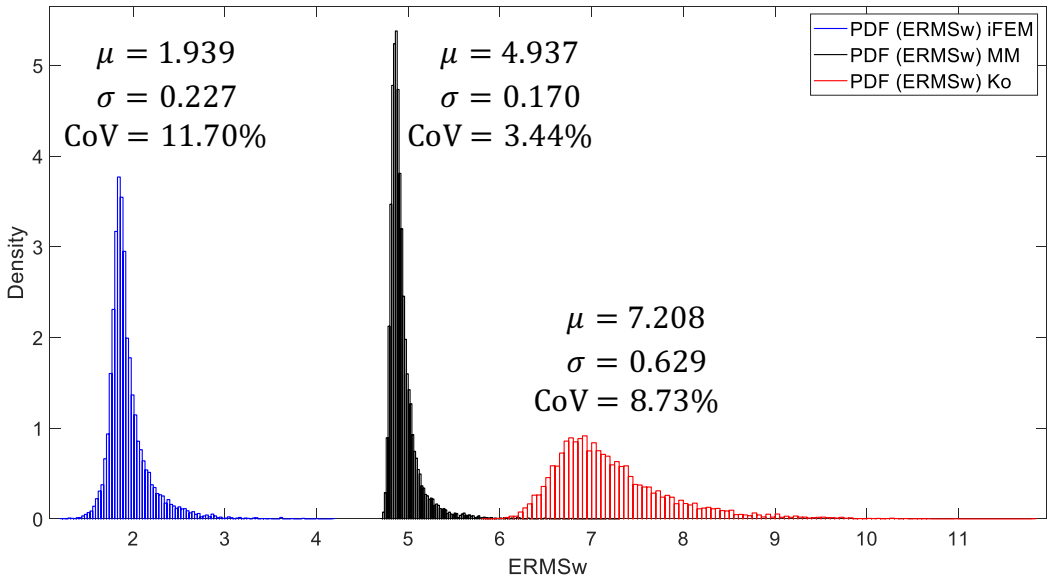

Figure 8: PDFs - Material uncertainty - Probability density functions of the $ERMSw$ obtained for the three shape sensing approaches with 10000 input vectors of material characteristics sampled with LHS.

In Figure 8, the discrete PDFs of the $ERMS_w$ of the three methods are plotted, along with the means, the standard deviations and the CoVs of the distributions. The means of all the distributions are close to the deterministic results, although they are slightly higher for all the three methods. The more peaked distribution is the one relative to the MM. The distribution corresponding to the iFEM is slightly less peaked, whereas the one relative to the Ko's Displacement theory is much flatter. Moreover, looking at the standard deviations, the same trend of variability for the three histograms can be inferred. The MM is found to be the less sensitive to the material uncertainty, exhibiting a really small influence of the input variability on the output. The iFEM shows a higher degree of variability, although it is important to notice that there is no overlapping between the worst result for the iFEM histogram and the best one for the MM one. Therefore, despite the fact that it is more affected by the material uncertainty, the iFEM is still able to perform better than the other two methods for any sample. The Ko's displacement theory is strongly influenced by the variability in the material characteristics. It is interesting to notice that the right side of the MM's graph extends so that it overlaps to the Ko's graph. It happens for a portion where the number of occurrences for the MM and the Ko's Displacement theory are really small. It means that, in some particular and rare conditions, the MM and the Ko's Displacement theory may perform with the same level of accuracy.

For the iFEM, an additional study on the influence of the penalization factors relative to the missing strain measurements, λ_{1-8}, was performed. The results for values of λ_{1-8} varying from 10^{-3} to 10^{-6} are reported in Figure 9. The distributions show that the penalization factors have a significant influence on the mean value of the distribution, whereas they have almost no influence on the standard deviation and on the PDFs. They are very similar to each other in shape and are only translated according to the different mean values. Therefore, it is proven that the λ_{1-8} coefficients don't have an influence on the variability of the displacements reconstruction due to the material uncertainty, whereas they have an influence on the deterministic accuracy of the method.

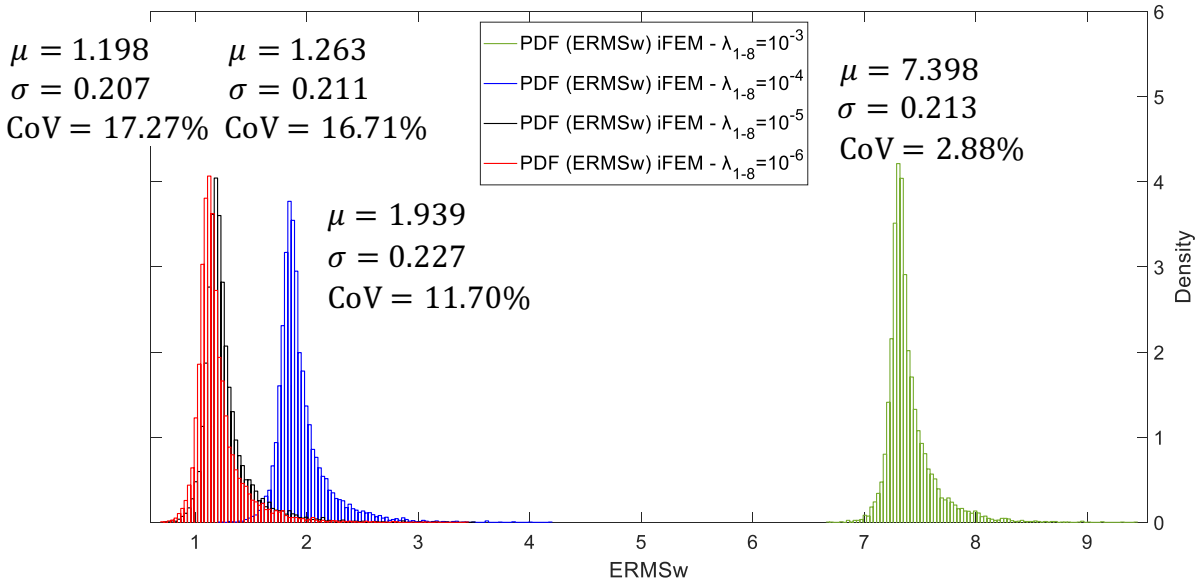

Figure 9: PDFs - Material uncertainty - Probability density functions of the $ERMSw$ obtained for the iFEM with varying λ_{1-8} values from 10^{-3} to 10^{-6}.

The second study, concerning the effect of the measurement noise, is now illustrated. A larger sample size of 30000 was established for the three methods, following the same convergence considerations described previously. The maximum variability in the CoV, when 50000 and 70000 samples were considered, was less than 2%, as reported in Table 5.

The outputs' PDFs resulting from the analyses with 5% and 10% normal errors in the strain measurements are reported in Figures 10 and 11, respectively. The peakedness of the distribution related to the MM is impressive. The 5% error has practically no effect in the $ERMS_w$ distribution and an almost negligible influence in the case of 10% error. On the other hand, the iFEM and Ko's Displacement theory show a more significant variability. When a 5% error is present, the two methods exhibit values of the standard deviations comparable to the ones obtained during the material analysis. These values appear approximately twice as big in the case of 10% error. The iFEM shows less variability and, in the two error scenarios, its histograms still never overlaps to the other two, showing better results for any occurrence. The overlapping between the MM and the Ko's Displacement theory's histograms is noticed when the normal error reaches the 10%, but this happens in the area where really small occurrence bars are present. The iFEM and Ko's histograms share another common feature, a nearly symmetric distribution with respect to the mean value. This feature indicates an equal possibility of having better or worst results with respect to the mean value. On the contrary, although with really lower variability, the MM's one is characterized by a highly positive skewness, only showing occurrences for solutions with a higher value of the $ERMS_w$ with respect to the mean one.

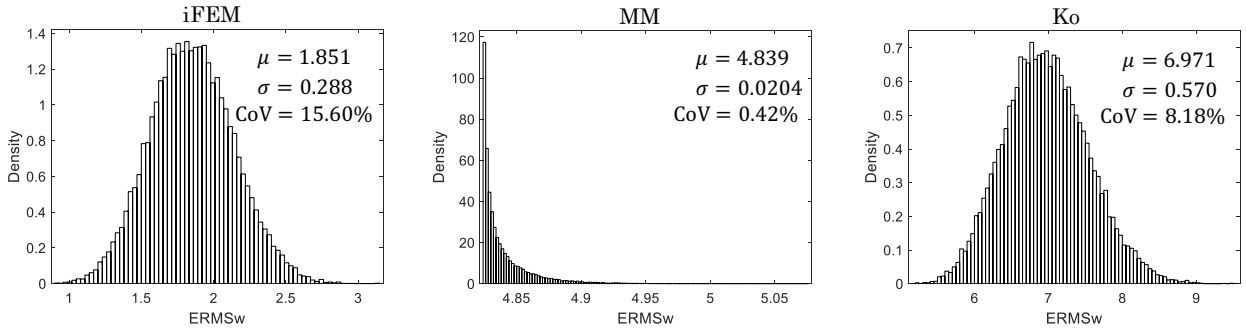

(a) iFEM (b) Modal Method (c) Ko's Displaecement theory

Figure 10: PDFs - Strain error 5% - Probability density functions of the $ERMSw$ obtained for the three shape sensing approaches with 30000 input vectors of strains affected by a normal error of 5%.

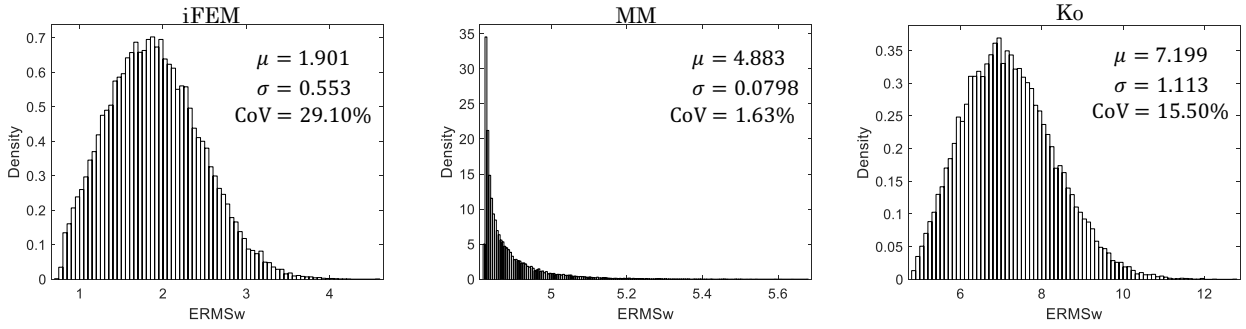

(a) iFEM (b) Modal Method (c) Ko's Displaecement theory

Figure 11: PDFs - Strain error 10% - Probability density functions of the $ERMSw$ obtained for the three shape sensing approaches with 30000 input vectors of strains affected by a normal error of 10%.

The effect of the strain measurement noise on the stress-field reconstruction has also been investigated for the three shape-sensing methods. Starting from the displacement field reconstructions and using the constitutive equations of the material, it is easy to compute the stress field that the structure is subject to. To compare the overall quality of the stress reconstruction, and taking into account the typical failure analysis relevant to multilayered composite structures, the Tsai-Hill failure index for composites has been chosen as a parameter to assess the global accuracy of the stress field reconstruction. To compute the Tsai- Hill index, the material strength properties reported in Table 6 have been used. The deterministic value of the maximum Tsai-Hill index, computed using the reference displacements from the high-fidelity model without any uncertainty in the system, is 0.73.

Table 6: Material strength characteristics.

Characteristic	**Value**
Longitudinal tensile strength	749 $[MPa]$
Longitudinal compressive strength	351 $[MPa]$
Transverse tensile strength	30 $[MPa]$
Transverse compressive strength	100 $[MPa]$
In-plane shear strength	25 $[MPa]$
Interlaminar shear strength	14 $[MPa]$

To study the influence of the measurement noise, the displacement field that have generated the PDFs in Figures 10 and 11 have been used to compute the percentage error, with respect to the deterministic value, of the reconstructed value of the maximum Tsai-Hill index. The obtained distributions are reported in Figures

12 and 13. The trend in the mean values of the error is the same noticed during the displacements analysis. The iFEM is the most accurate of the three method. Moreover, in this case, the advantage in the accuracy in favor of the iFEM is even more remarkable. The mean values of the estimations of the Tsai-Hill index for the MM and the Ko's Displacement theory are highly inaccurate. The standard deviations of the distributions relative to the three methods are comparable and also the CoVs are closer than in the shape sensing case. As a consequence, the higher robustness of the MM, in particular with respect to the iFEM, is still exhibited but less marked.

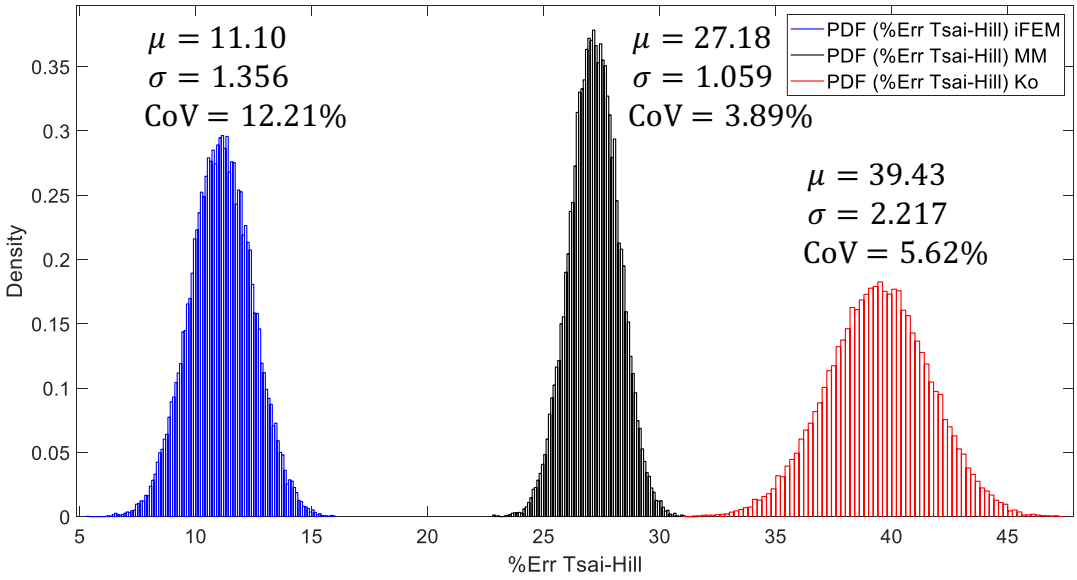

Figure 12: PDFs - Strain error 5% - Probability density functions of the percentage error (%Err Tsai-Hill) in the reconstruction of the maximum Tsai-Hill failure index.

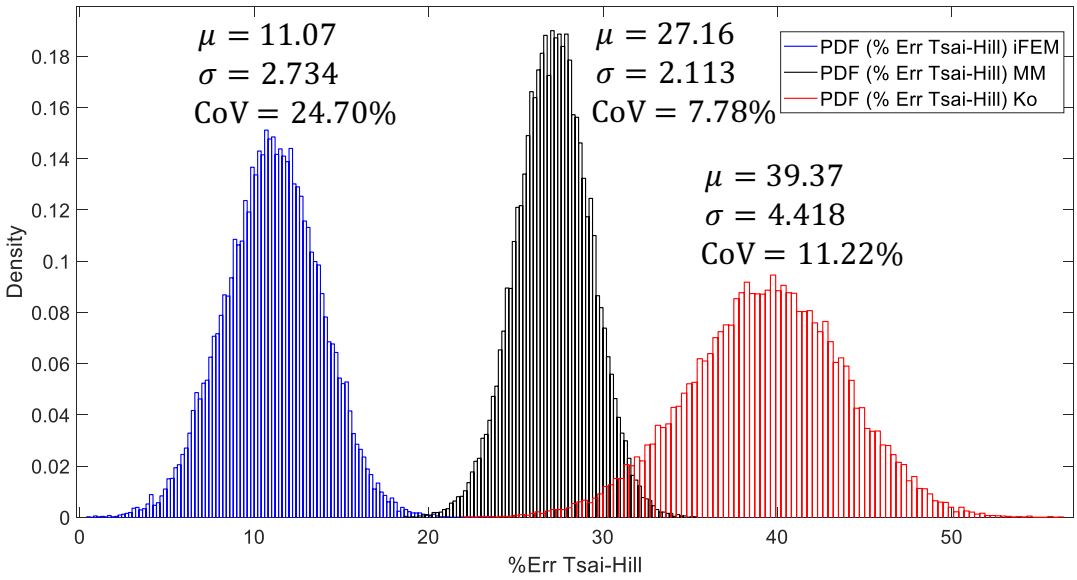

Figure 13: PDFs - Strain error 10% - Probability density functions of the percentage error (%Err Tsai-Hill) in the reconstruction of the maximum Tsai-Hill failure index.

6 Conclusions

This paper investigated the influence of uncertain material properties and noisy strain measurements on the outputs of three shape sensing methods, the inverse Finite Element Method, the Modal Method and the Ko's Displacement theory. The three methods have been applied to the reconstruction of the deformed shape of a composite wing box undergoing a bending and torsional deformation. The uncertainties have been introduced after optimizing the strain sensors set-up for the three methods, so that their effect on the performances of the methods could be compared when each method performed at its highest level of accuracy. The optimization of the sensors configurations have been performed during the deterministic analysis, before any kind of uncertainty was introduced into the problem.

The composite material modelization is strongly influenced by the deviation of the real characteristics from the nominal ones. In this work, the uncertainties related to the composite material were studied at the ply level by performing a Monte Carlo Simulation. The ply thickness, the fibre orientations and the lamina mechanical properties were sampled from normal distributions centered in their nominal values, using the Latin Hypercube Sampling. Performing the shape sensing analysis for the different input values, it has been possible to compute the PDFs of the RMS percent errors between the reference vertical displacements and the reconstructed ones ($ERMS_w$). These outputs' distributions proved that the MM is the most robust with respect to the material uncertainties. The iFEM, that showed the best results during the deterministic analysis, is more influenced by the material uncertainties, but it is still capable of a better reconstruction of the displacement field for every sample, meaning that in its worst case scenario, when the uncertainties have the most negative influence on the output, iFEM is still more accurate than MM. The Ko's Displacement theory, that was the less accurate according to the deterministic analysis, also showed a high variability caused by the material properties uncertainties.

The other cause of uncertainty that can influence the performance of the shape sensing is represented by the noise that can affect the strain measurements. To take into account these effects, the same Monte Carlo approach has been used. A Gaussian error of 5% and 10% of the nominal strain values was sampled with LHS and added to the strain inputs for the three shape sensing methods. The distributions of the $ERMS_w$ confirmed the results obtained during the material uncertainty analysis. For both the levels of the Gaussian error, the MM's output is barely influenced by this kind of inputs' variability. Once again, the iFEM distribution is moderately affected by the presence of uncertain inputs, whereas the Ko's displacement theory shows a more relevant variability in the output.

This work also investigated the effect of the measurement noise on the reconstruction of Tsai-Hill failure index, computed by means of the stress-displacement constitutive equations. In this case the robustness of the three methods is comparable and the MM results only slightly less influenced by the inputs' variability. Moreover, the iFEM shows a significantly higher overall accuracy in the reconstruction of the Tsai-Hill index.

In conclusion, the MM is the shape sensing method that is less influenced by the various source of uncertainties. Therefore, the MM represents a useful tool when there is no confidence in the knowledge of the material characteristics or the strain measurements. Moreover, the MM requires a smaller number of sensors than the iFEM. The iFEM is more sensitive, but the cases most negatively influenced by the uncertainties are still capable of a greater accuracy than the best one from MM. As a consequence, when more accuracy is required and more sensors are available, the iFEM is still to be preferred. The Ko's Displacement theory is not suitable when uncertainty is present. The high variability in the output prevents from confidently rely on the obtained results. Finally, when a study on the stress field reconstruction is also involved, the iFEM is strongly recommended over the other two methods.

This work is part of a broad study on the application of shape sensing techniques to aircraft structures. After having compared the performance of three shape sensing methods on the reconstruction of the deformed shape of a composite wing box, in this work, the influence of an uncertain structural behavior has been introduced and analyzed. The next step of the investigation should involve the experimental validation on a real wing box of the previous studies.

To further expand the knowledge about the behavior of the shape sensing methods in experimental scenarios affected by uncertainty, future works should also investigate the robustness of the optimal sensors configuration by means of the robust optimization framework.

Acknowledgments:
Computational resources were provided by HPC@POLITO, a project of Academic Computing within the Department of Control and Computer Engineering at the Politecnico di Torino (`http://www.hpc.polito.it`).

References

[1] Brian J. Soller, Dawn K. Gifford, Matthew S. Wolfe, and Mark E. Froggatt. High resolution optical frequency domain reflectometry for characterization of components and assemblies. *Opt. Express*, 13(2):666–674, Jan 2005.

[2] Raffaella Di Sante. Fibre optic sensors for structural health monitoring of aircraft composite structures: Recent advances and applications. *Sensors*, 15(8):18666–18713, 2015.

[3] L. Colombo, C. Sbarufatti, and M. Giglio. Definition of a load adaptive baseline by inverse finite element method for structural damage identification. *Mechanical Systems and Signal Processing*, 120:584 – 607, 2019.

[4] Rinto Roy, Marco Gherlone, and Cecilia Surace. Damage localisation in thin plates using the inverse finite element method. In Magd Abdel Wahab, editor, *Proceedings of the 13th International Conference on Damage Assessment of Structures*, pages 199–212, Singapore, 2020. Springer Singapore.

[5] Mingyang Li, Adnan Kefal, Burak Can Cerik, and Erkan Oterkus. Dent damage identification in stiffened cylindrical structures using inverse finite element method. *Ocean Engineering*, 198:106944, 2020.

[6] Luca Colombo, Daniele Oboe, Claudio Sbarufatti, Francesco Cadini, Salvatore Russo, and Marco Giglio. Shape sensing and damage identification with ifem on a composite structure subjected to impact damage and non-trivial boundary conditions. *Mechanical Systems and Signal Processing*, 148:107163, 2021.

[7] Fred Austin, Michael J. Rossi, William Van Nostrand, Gareth Knowles, and Antony Jameson. Static shape control for adaptive wings. *AIAA Journal*, 32(9):1895–1901, 1994.

[8] Andreea Koreanschi, Oliviu Sugar Gabor, Joran Acotto, Guillaume Brianchon, Gregoire Portier, Ruxandra Mihaela Botez, Mahmoud Mamou, and Youssef Mebarki. Optimization and design of an aircraft's morphing wing-tip demonstrator for drag reduction at low speeds, part ii - experimental validation using infra-red transition measurement from wind tunnel tests. *Chinese Journal of Aeronautics*, 30(1):164 – 174, 2017.

[9] Maurizio Arena, Francesco Amoroso, Rosario Pecora, Gianluca Amendola, Ignazio Dimino, and Antonio Concilio. Numerical and experimental validation of a full scale servo-actuated morphing aileron model. *Smart Materials and Structures*, 27(10):105034, sep 2018.

[10] Rolf Evenblij, Frank Kong, Christos Koimtzoglou, Monica Ciminello, Ignazio Dimino, and Antonio Concilio. Shape sensing for morphing structures using fiber bragg grating technology. In Piet Christof Wölcken and Michael Papadopoulos, editors, *Smart Intelligent Aircraft Structures (SARISTU)*, pages 471–491, Cham, 2016. Springer International Publishing.

[11] William L. Ko, W. Lance Richards, and Van T. Fleischer. Displacement theories for in-flight deformed shape predictions of aerospace structures. Report NASA/TP-2007-214612, NASA Dryden Flight Research Center; Edwards, CA, United States, 2007.

[12] G. C. Foss and E. D. Haugse. Using Modal Test Results to Develop Strain to Displacement Transformations. In *Proceedings of the 13th International Modal Analysis Conference*. Nashville, 1995.

[13] Attilio C. Pisoni, Claudio Santolini, Dagmar E. Hauf, and Steven Dubowsky. Displacements in a vibrating body by strain gauge measurements. In *Proceedings of the 13th International Modal Analysis Conference*. Nashville, 1995.

[14] Chen-Jung Li and A.Galip Ulsoy. High-precision measurement of tool-tip displacement using strain gauges in precision flexible line boring. *Mechanical Systems and Signal Processing*, 13(4):531–546, 1999.

[15] Alexander Tessler and Jan L. Spangler. A variational principal for reconstruction of elastic deformation of shear deformable plates and shells. Report NASA/TM-2003-212445, NASA Langley Research Center, Hampton, VA, United States, 2003.

[16] William L. Ko, W. Lance Richards, and Van T. Fleischer. Applications of the ko displacement theory to the deformed shape predictions of the doubly-tapered ikhana wing. Report NASA/TP-2009-214652, NASA Dryden Flight Research Center; Edwards, CA, United States, 2009.

[17] Christine V. Jutte, William L. Ko, Craig A. Stephens, John A. Bakalyar, and W. Lance Richards. Deformed shape calculation of a full-scale wing using fiber optic strain data from a ground loads test. Report NASA/TP-2011-215975, NASA Dryden Flight Research Center; Edwards, CA, United States, 2011.

[18] Guoping Ding, Shengyuan Yue, Songchao Zhang, and Wenhao Song. Strain - deformation reconstruction of cfrp laminates based on ko displacement theory. *Nondestructive Testing and Evaluation*, 0(0):1–13, 2020.

[19] Cheng Xu and Zahra Sharif Khodaei. Shape sensing with rayleigh backscattering fibre optic sensor. *Sensors*, 20(14), 2020.

[20] Chan Pak. Wing shape sensing from measured strain. *AIAA Journal*, 54(3):1068–1077, 2016.

[21] J. C. O'Callahan, P. Avitabile, and R. Riemer. System equivalent reduction expansion process. In *Proc. of the 7th Inter. Modal Analysis Conf.* Las Vegas, 1989.

[22] Christopher Chipman and Peter Avitabile. Expansion of transient operating data. *Mechanical Systems and Signal Processing*, 31:1 – 12, 2012.

[23] Philip Bogert, Eric Haugse, and Ralph Gehrki. Structural shape identification from experimental strains using a modal transformation technique. In *44th AIAA/ASME/ASCE/AHS/ASC Structures, Structural Dynamics, and Materials Conference*. Norfolk, 2012.

[24] Maxim Freydin, Miko Keren Rattner, Daniella E. Raveh, Iddo Kressel, Roy Davidi, and Moshe Tur. Fiber-optics-based aeroelastic shape sensing. *AIAA Journal*, 57(12):5094–5103, 2019.

[25] Marco Gherlone, Priscilla Cerracchio, Massimiliano Mattone, Marco Di Sciuva, and Alexander Tessler. Shape sensing of 3d frame structures using an inverse finite element method. *International Journal of Solids and Structures*, 49(22):3100 – 3112, 2012.

[26] Marco Gherlone, Priscilla Cerracchio, Massimiliano Mattone, Marco Di Sciuva, and Alexander Tessler. An inverse finite element method for beam shape sensing: theoretical framework and experimental validation. *Smart Materials and Structures*, 23(4):045027, mar 2014.

[27] Alexander Tessler and Jan L. Spangler. Inverse fem for full-field reconstruction of elastic deformations in shear deformable plates and shells. In *Proceedings of the 2nd European Workshop on Structural Health Monitoring*. Munich, 2004.

[28] Umberto Papa, Salvatore Russo, Angelo Lamboglia, Giuseppe Del Core, and Generoso Iannuzzo. Health structure monitoring for the design of an innovative uas fixed wing through inverse finite element method (ifem). *Aerospace Science and Technology*, 69:439 – 448, 2017.

[29] Alexander Tessler, Rinto Roy, Marco Esposito, Cecilia Surace, and Marco Gherlone. Shape sensing of plate and shell structures undergoing large displacements using the inverse finite element method. *Shock and Vibration*, 8076085:8 pages, 2018.

[30] Priscilla Cerracchio, Marco Gherlone, and Alexander Tessler. Real-time displacement monitoring of a composite stiffened panel subjected to mechanical and thermal loads. *Meccanica*, 50:2487–2496, 2015.

[31] Eric J. Miller, Russel Manalo, and Alexander Tessler. Full-field reconstruction of structural defor- mations and loads from measured strain data on a wing using the inverse finite element method. Report NASA/TM-2016-219407, NASA Dryden Flight Research Center; Edwards, CA United States, 2016.

[32] Adnan Kefal, Erkan Oterkus, Alexander Tessler, and Jan L. Spangler. A quadrilateral inverse-shell element with drilling degrees of freedom for shape sensing and structural health monitoring. *Engineering Science and Technology, an International Journal*, 19(3):1299 – 1313, 2016.

[33] Adnan Kefal and Erkan Oterkus. Displacement and stress monitoring of a chemical tanker based on inverse finite element method. *Ocean Engineering*, 112:33 – 46, 2016.

[34] Adnan Kefal and Erkan Oterkus. Displacement and stress monitoring of a panamax containership using inverse finite element method. *Ocean Engineering*, 119:16 – 29, 2016.

[35] Marco Esposito and Marco Gherlone. Composite wing box deformed-shape reconstruction based on measured strains: Optimization and comparison of existing approaches. *Aerospace Science and Technology*, 99:105758, 2020.

[36] Feifei Zhao, Libo Xu, Hong Bao, and Jingli Du. Shape sensing of variable cross-section beam using the inverse finite element method and isogeometric analysis. *Measurement*, 158:107656, 2020.

[37] Adnan Kefal and Erkan Oterkus. Isogeometric ifem analysis of thin shell structures. *Sensors*, 20(9), 2020.

[38] Adnan Kefal, Isa Emami Tabrizi, Mehmet Yildiz, and Alexander Tessler. A smoothed ifem approach for efficient shape-sensing applications: Numerical and experimental validation on composite structures. *Mechanical Systems and Signal Processing*, 152:107486, 2021.

[39] Srinivas Sriramula and Marios K. Chryssanthopoulos. Quantification of uncertainty modelling in stochastic analysis of frp composites. *Composites Part A: Applied Science and Manufacturing*, 40(11):1673 – 1684, 2009.

[40] B. Navaneetha Raj, N.G.R. Iyengar, and D. Yadav. Response of composite plates with random material properties using fem and monte carlo simulation. *Advanced Composite Materials*, 7(3):219–237, 1998.

[41] H.K. Jeong and R.A. Shenoi. Probabilistic strength analysis of rectangular frp plates using monte carlo simulation. *Computers & Structures*, 76(1):219 – 235, 2000.

[42] T.S. Mesogitis, A.A. Skordos, and A.C. Long. Uncertainty in the manufacturing of fibrous thermosetting composites: A review. *Composites Part A: Applied Science and Manufacturing*, 57:67 – 75, 2014.

[43] M. D. McKay, R. J. Beckman, and W. J. Conover. A comparison of three methods for selecting values of input variables in the analysis of output from a computer code. *Technometrics*, 21(2):239–245, 1979.

[44] Alda Carvalho, Tiago A.N. Silva, and Maria A.R. Loja. Assessing static and dynamic response variability due to parametric uncertainty on fibre-reinforced composites. *Journal of Composites Science*, 2(1), 2018.

[45] Mishal Thapa, Sameer B. Mulani, and Robert W. Walters. Stochastic multi-scale modeling of carbon fiber reinforced composites with polynomial chaos. *Composite Structures*, 213:82 – 97, 2019.

[46] Marco Gherlone, Priscilla Cerracchio, and Massimiliano Mattone. Shape sensing methods: Review and experimental comparison on a wing-shaped plate. *Progress in Aerospace Sciences*, 99:14 – 26, 2018.

[47] W Montero, R Farag, V Díaz, M Ramirez, and B L Boada. Uncertainties associated with strain-measuring systems using resistance strain gauges. *The Journal of Strain Analysis for Engineering Design*, 46(1):1–13, 2011.

[48] Jérémy Arpin-Pont, Martin Gagnon, Antoine S Tahan, André Coutu, and Denis Thibault. Methodology for estimating strain gauge measurement biases and uncertainties on isotropic materials. *The Journal of Strain Analysis for Engineering Design*, 50(1):40–50, 2015.

[49] Adnan Kefal, Jimmy Bunga Mayang, Erkan Oterkus, and Mehmet Yildiz. Three dimensional shape and stress monitoring of bulk carriers based on ifem methodology. *Ocean Engineering*, 147:256 – 267, 2018.

[50] R.D. Mindlin. Influence of rotatory inertia and shear deformation on flexural motions of isotropic elastic plates. *Journal of Applied Mechanics*, 18:31 – 138, 1951.

[51] A. Tessler, J.L. Spangler, M. Gherlone, M. Mattone, and Marco Di Sciuva. Real-time characterization of aerospace structures using onboard strain measurement technologies and inverse finite element method. In *Proceedings of the 8th International Workshop on Structural Health Monitoring*. Stanford, 2011.

[52] M. D. Mckay, R. J. Beckman, and W. J. Conover. A comparison of three methods for selecting values of input variables in the analysis of output from a computer code. *Technometrics*, 42(1):55–61, 2000.

[53] Manuele Corradi, Marco Gherlone, Massimiliano Mattone, and Marco Di Sciuva. *A Comparative Study of Uncertainty Propagation Methods in Structural Problems*, pages 87–111. Springer Netherlands, Dordrecht, 2013.